Chinese Chemical Letters 37 (2026) 111569

Contents lists available at ScienceDirect

Chinese Chemical Letters

journal homepage: www.elsevier.com/locate/cclet

Nanozyme with dual enzyme activity mediating cascade catalytic therapy synergize multiple functions for antitumor therapy

Dou Zhang[a,b], Xinyi Cai[a,b], Yimin Li[c], Yong Liu[a,b], Long Qiu[a,b], Zhenying Diao[a,b], Xuyi Liu[a,b], Yuta Nishina[d], Yajuan Zou[d], Jianbo Sun[a], Shujing Liang[e,*], Daxiang Cui[a,b,f,*], Ting Yin[a,b,*]

[a] Research Center of Nano Technology and Application Engineering, The First Dongguan Affiliated Hospital, School of Pharmacy, Guangdong Medical University, Dongguan 523808, China
[b] Dongguan Research Center for Biomedical Nano Engineering Technology Research, Guangdong Medical University, Dongguan 523808, China
[c] The First Clinical College of Jinan University, Guangzhou 510632, China
[d] Research Institute for Interdisciplinary Science, Okayama University, 3-1-1 Tsushimanaka, Kita-ku, Okayama 700-8530, Japan
[e] Department of Oncology, East Hospital Affiliated to Tongji University, Tongji University School of Medicine, Tongji University, Shanghai 200092, China
[f] School of Sensing Science and Engineering, School of Electronic Information and Electrical Engineering, Shanghai Jiao Tong University, Shanghai 200240, China

ARTICLE INFO

Article history:
Received 29 April 2025
Revised 7 July 2025
Accepted 9 July 2025
Available online 10 July 2025

Keywords:
Nanozyme
Catalytic therapy
Chemodynamic therapy
Synergistic therapy
Immunogenic cell death

ABSTRACT

Nanozymes-mediated catalytic therapy is an emerging approach for tumor treatment, but the performance of the nanozymes is limited by low enzyme catalytic efficiency, low reaction substrate concentration, and immunosuppressive features of the tumor microenvironment. Herein, a hollow gold nanorods loaded with oxygen-carrying hemoglobin ($HAuHbO_2$) nanozyme with high enzyme catalytic efficiency is reported. In the tumor microenvironment, $HAuHbO_2$ shows dual enzyme activities of glucose oxidase (GOD) and peroxidase (POD) for spontaneous cascade catalytic reactions to realize chemodynamic therapy (CDT). Meanwhile, it exerts excellent photothermal conversion ability for photothermal therapy (PTT). This study also reports the antitumor ability of $HAuHbO_2$, including its mechanism of action *in vivo*. $HAuHbO_2$ can induce the occurrence of immunogenic cell death (ICD) with the involvement of near-infrared light, which in turn induces the immune response of the organism. Overall, a simple, ingenious, and multifunctional nanozyme is designed in this study, which can provide a basis for applying nanozymes in antitumor therapy.

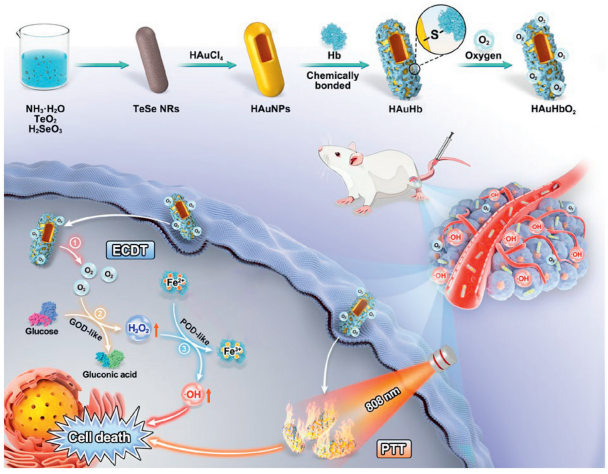
© 2025 Published by Elsevier B.V. on behalf of Chinese Chemical Society and Institute of Materia Medica, Chinese Academy of Medical Sciences.

Natural enzymes are important functional substances in organisms. They also play an indispensable role in genesis and survival of tumor [1–3]. Metabolic changes caused by natural enzymes during tumor development cannot be ignored, such as large production of proteins [4], lipids [5] and nucleic acids [6] as well as consumption of energy substances such as carbohydrates [2,7]. Therefore, targeting natural enzymes is an effective strategy for tumor treatment [8,9]. Factors such as substrate and enzyme concentration during enzyme reaction will promote tumor cell death [10,11]. However, the levels of natural enzymes in organisms are extremely low, the influencing factors are difficult to regulate [12], and the synthesis of natural enzymes is limited by complex spatial structures, cumbersome synthesis processes, expensive production costs, and specific storage conditions [13,14]. Hence, nanozymes have been developed to overcome these difficulties and meet the needs of tumor therapy.

Nanozymes are synthesized artificially and possess the properties of nanomaterials and catalytic functions of enzymes [15]. Compared with natural enzymes, nanozymes have simpler structures, easier preparation and easier storage. Under physiological conditions, nanozymes follow the same kinetic mechanism as natural enzymes and can effectively catalyze the conversion of substrates. Surprisingly, some nanozymes with specific structures can exert multiple enzymatic activities. Their excellent catalytic efficiency and biocompatibility open a new field for applying nanozymes in tumor therapy [16,17]. In tumor sites, nanozymes use metabolites in the tumor microenvironment as substrates and catalyze the generation of active substances with properties that lead to cell death [18]. In addition, nanozymes can be used as carriers to deliver con-

* Corresponding authors.
E-mail addresses: liangshujing02@126.com (S. Liang), dxcui@sjtu.edu.cn (D. Cui), wsyt132@163.com (T. Yin).

https://doi.org/10.1016/j.cclet.2025.111569
1001-8417/© 2025 Published by Elsevier B.V. on behalf of Chinese Chemical Society and Institute of Materia Medica, Chinese Academy of Medical Sciences.



Scheme 1. Schematic illustrations of nanozyme ($HAuHbO_2$) for tumor treatment, including the preparation and therapeutic mechanisms.

ventional drugs to the tumor site. In combination with the properties of the nanomaterials themselves, nanocatalytic therapies are also often combined with other therapies to produce detrimental effects to tumor cells, such as photothermal therapy (PTT), sonodynamic therapy (SDT), photodynamic therapy (PDT), and chemical-dynamic therapy (CDT). Despite the excellent catalytic properties of nanozymes, the lack of reaction substrates in the tumor microenvironment and the limitation of reaction conditions prevent the advantages of nanozymes from being fully exploited [19]. Therefore, there is an urgent need to develop nanozyme systems with reaction substrates and conditions.

Here, a nanozyme ($HAuHbO_2$) consists of hollow gold nanorods (HAuNPs) loaded with oxygen-carrying hemoglobin (HbO_2) was designed to achieve antitumor therapy by spontaneous cascade catalytic function under near-infrared (NIR) radiation (Scheme 1). The glucose oxidase (GOD)-like and peroxidase (POD)-like activities of $HAuHbO_2$ can effectively catalyze the production of cytotoxic $^{\bullet}OH$ in the tumor microenvironment and stimulate tumor cell death. The anti-tumor experiments results indicate that $HAuHbO_2$ is an effective therapeutic reagent. More importantly, $HAuHbO_2$ have good biosafety. In summary, the study could provide a new understanding of the role of nanozymes in tumor therapy (Table S1 in Supporting information).

$HAuHbO_2$ is prepared by binding sulfhydryl groups on HAuNPs and Hb to form disulfide bonds. The stability of HAuNPs and the biological activity of Hb were both well preserved, which was confirmed by the following experiments. First, transmission electron microscopy (TEM) was used to demonstrate the morphological features of the nanozyme. The rod-like morphology of TeSe, HAuNPs and $HAuHbO_2$ can be visualized clearly in Fig. 1a. The hollow structure of HAuNPs increases the surface area of the material, making it an effective carrier. A thin film can be visualized on the surface of $HAuHbO_2$ demonstrating the successful loading Hb onto the HAuNPs. Additionally, elemental mapping further analyzes the composition of $HAuHbO_2$ at Fig. 1b. The characteristic absorption peaks of Hb, HAuNPs, and $HAuHbO_2$ were measured by ultraviolet-visible (UV–vis) spectrophotometer (Fig. 1c). $HAuHbO_2$ was found to have characteristic peaks of Hb and HAuNPs, indicating the successful construction of the nanozyme. The hydrodynamic sizes of HAuNPs and $HAuHbO_2$ are shown in Fig. 1d, which are 125 and 170 nm, respectively. It indicates that the particle size is increasing from HAuNPs to $HAuHbO_2$. In addition, it was determined in Fig. 1e that the zeta potentials of Hb, HAuNPs, and $HAuHbO_2$ were −1.06, −5.96, and −2.48 mV, respectively. These experimental results confirmed the successful preparation of the nanozyme and

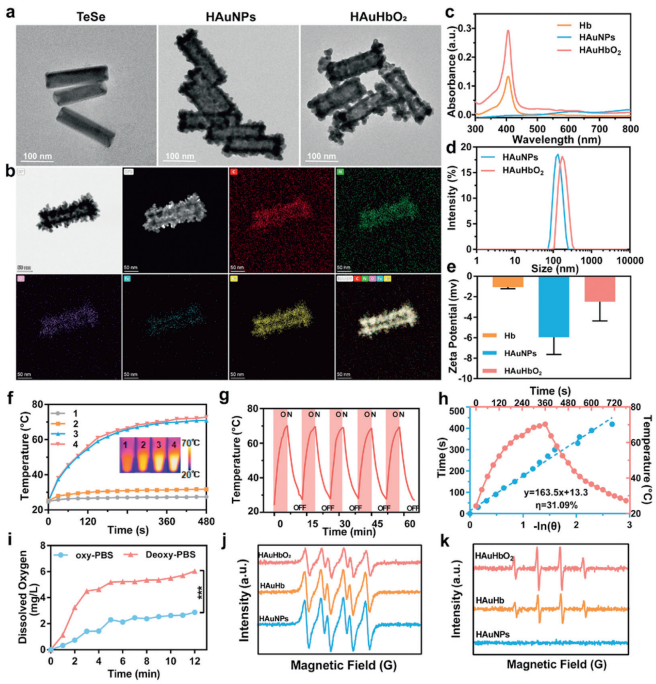


Fig. 1. Preparation and characterization of $HAuHbO_2$. (a) TEM images of TeSe nanorods, HAuNPs and $HAuHbO_2$. Scale bar: 100 nm. (b) Element mapping of $HAuHbO_2$. Scale bar: 50 nm. (c) UV–vis absorption spectra of Hb, HAuNPs, $HAuHbO_2$. (d) Hydrodynamic diameter of HAuNPs and $HAuHbO_2$. (e) Zeta potential of Hb, HAuNPs, and $HAuHbO_2$. Data were presented as means ± standard error of the mean (SEM) ($n = 3$). (f) The heating curves of PBS (1), Hb (2), HAuNPs (3), and $HAuHbO_2$ (4) under laser. The inset represents their infrared imaging. (g) Temperature profiles of $HAuHbO_2$ under five laser on/off cycles. (h) Calculation of the photothermal conversion capacity of $HAuHbO_2$. (i) Dissolved oxygen curves of $HAuHbO_2$ in different solutions. (j) The generation of H_2O_2 was assessed by EPR. (k) The generation of $^{\bullet}OH$ was detected by EPR.

revealed the potential functions, including PTT and photoacoustic (PA) imaging.

In order to demonstrate the potential of $HAuHbO_2$ as a PTT agent, the photothermal effect was investigated by monitoring the thermal activities with 808 nm (1.0 W/cm^2) continuous laser irradiation. As shown in Fig. 1f, phosphate buffered saline (PBS) showed the lowest response to laser. Notably, Hb exhibited photothermal properties under the same experimental conditions. It is consistent with the conclusions of previous studies that Hb has photothermal conversion ability [20,21]. Therefore, the final temperature of $HAuHbO_2$ was higher than HAuNPs. The photothermal images of the four samples after laser are shown in Fig. 1f. In addition, when subjected to five heating/cooling cycles, the temperature change of $HAuHbO_2$ remained stable (Fig. 1g). It demonstrated the good photothermal stability of $HAuHbO_2$. The photothermal conversion efficiency (η) was calculated to be as high as 31.09 % under 808 nm irradiation (Fig. 1h). The good photothermal stability and conversion efficiency of $HAuHbO_2$ make it a potential PTT for tumor therapy.

As Hb has the function of oxygen carrier, its oxygen carrying capacity was also verified here. As shown in Fig. S1 (Supporting information), oxygen content in deoxy-PBS, HAuHb and $HAuHbO_2$ solutions was measured. The result shows that $HAuHbO_2$ had the highest dissolved oxygen, indicating its oxygen carrying capacity. In addition, the oxygen carrying stability of $HAuHbO_2$ was also evaluated. As shown in Fig. 1i, deoxy-PBS simulates an anoxic tumor microenvironment, releasing oxygen rapidly after nanozyme enters the solution, and then maintaining a stable oxygen release rate. This experiment provides evidence for the function of nanozyme in alleviating hypoxia in tumor therapy. The hydrodynamic diameter of $HAuHbO_2$ remained stable without any substantial change in

water, PBS, and DMEM for 7 days (Fig. S2 in Supporting information), which indicated its good stability.

The enzyme mimetic activities of the nanozymes were evaluated using the electron paramagnetic resonance (EPR) technique. First, the generation of H_2O_2 was verified. In the system of glucose mixed with nanozymes, the generated superoxide hydroxyl radical ($^{\bullet}O_2^-$) gradually evolved into superoxide hydroxyl radical ($^{\bullet}OOH$) as the reaction proceeded and was rapidly converted to H_2O_2 by protonation [22]. The EPR system focused on the intermediate reactive species $^{\bullet}O_2^-$ in the pathway of H_2O_2 generation. Fig. 1j demonstrates the ability of HAuNPs, HAuHb, and $HAuHbO_2$ to generate $^{\bullet}O_2^-$. Three samples showed the possibility that H_2O_2 was generated. It is noteworthy that the strongest signal was found in the HAuNPs, which may be the H_2O_2 in HAuHb and $HAuHbO_2$ had already reacted in the later step. After subjecting the reaction system to laser irradiation, the catalytic efficiency of HAuNPs was found to be significantly improved (Fig. S3 in Supporting information), whereas no signals were detected in the HAuHb and $HAuHbO_2$, which inferred that the generated H_2O_2 had already been engaged in the subsequent reaction. The occurrence of the second-step reaction was also investigated. As shown in Fig. 1k, the nanozymes exhibited significant $^{\bullet}OH$ generation. The characteristic signal of $^{\bullet}OH$ appeared in the glucose and nanozyme mixed system. It was not detected in the component HAuNPs system alone, implying the lack of POD-like activity without Hb. Similarly, the signal enhancement upon laser irradiation indicates that light can facilitate the reaction (Fig. S4 in Supporting information). Compared with HAuHb and $HAuHbO_2$, adding more oxygen was seen to promote the reaction. In conclusion, these results strongly demonstrate the enzyme catalytic activities of the nanozyme with GOD and POD, which further extend the therapeutic potentials for tumor treatment.

Different experimental approaches were further used to evaluate enzyme mimetic properties. HAuNPs catalyze glucose and O_2 into gluconic acid and H_2O_2 (Fig. 2a). H_2O_2 generation was detected using indigo carmine (IC) as an indicator. As shown in Fig. 2b, the absorbance of IC was the highest but was the lowest in HAuNPs+IC. It indicated that HAuNPs catalyzed the generation of H_2O_2. Meanwhile, the absorbance of $HAuHbO_2$+IC was also reduced but larger than HAuNPs+IC. It is caused by the Fenton reaction, which consumed H_2O_2 in the system. The color changes of IC can be seen in the photo at the upper right of the UV map. Subsequently, the kinetics of the GOD-like reaction of HAuNPs was investigated (Fig. 2c). It was shown that the K_m of HAuNPs was 5.972 mmol/L, and the catalytic efficiency (kcat/km) could reach 849.4 L mol^{-1} s^{-1}.

The mechanism of POD-like activity was subsequently revealed. 3,3′,5,5′-Tetramethylbenzidine (TMB) is a commonly used probe for ·OH detection (Fig. 2d). Fig. 2e shows no significant absorption was observed in TMB, TMB+Glu and $HAuHbO_2$. However, a clear absorption peak at 652 nm was observed in TMB+Glu+$HAuHbO_2$, which indicating that the production of $^{\bullet}OH$. This difference is also illustrated by the apparent change in color between solutions. The effects of glucose and $HAuHbO_2$ concentrations on the cascade reactions were also verified (Figs. 2f and g). Fig. 2h shows the effect of laser irradiation to catalytic reaction, which is consistent with the results of EPR. The POD-like reaction kinetics of $HAuHbO_2$ were also investigated (Fig. 2i). The results showed the catalytic kinetics of $HAuHbO_2$ ($K_m = 51.36$ mmol/L, $V_{max} = 1.76 \times 10^{-6}$ mol L^{-1} s^{-1}).

Finally, the mechanism of the GOD-like catalytic activity was explored by density functional theory (DFT). When glucose is not added by a catalyst to produce H_2O_2, external energy must be added (Fig. S5 in Supporting information), which limits the production of H_2O_2 in the natural state. Two nanoclusters, Au(III) and Au_{38}, were considered for the study of the catalytic interface (Fig. S6 in Supporting information). In the reaction system, glucose molecules and O_2 are first adsorbed on the gold nanoclusters, and then -Hs on the glucose molecules are transferred to O_2 to finally form H_2O_2. The energy changes during this reaction are shown in Fig. 2j. When Au(III) was used as the catalytic surface, O_2 was dispersed near the glucose, and then two O atoms of glucose and O_2 were bound to the Au surface sites, respectively. Then, -Hs on glucose are transferred to O_2 to generate the complex $C_6H_{11}O_6$*_OOH* (* indicates the adsorption state). -OOH is favorable on the Au surface and can break the two hydrogen bonds between -OOH and $C_6H_{11}O_6$ by rotating -OOH*. The process absorbs heat and transfers it. Upon -OOH transfer, another H atom on the glucose molecule spontaneously dissociates and moves toward the -OOH to form H_2O_2 (Fig. S7 in Supporting information). Overall, the process that produces H_2O_2 is kinetically and thermodynamically favorable, with the rate-limiting step forming the $C_6H_{11}O_6$-OOH complex. In contrast, the catalytic process on the Au_{38} surface requires less energy. Unlike Au(III), the adsorption of glucose onto the Au_{38} surface requires energy absorption from the outside. Moreover, only one O atom in O_2 is adsorbed on the Au_{38} surface (Fig. S8 in Supporting information). Compared with Au(III), a smaller energy change occurs in the process of -OOH breaking during Au_{38} catalysis. Therefore, it is conceivable that Au_{38} exhibits a faster reaction rate. These data indicate that $HAuHbO_2$ has an excellent enzymatic activity, which will provide a basis for its remarkable therapeutic effect in tumor microenvironment (Fig. 2k).

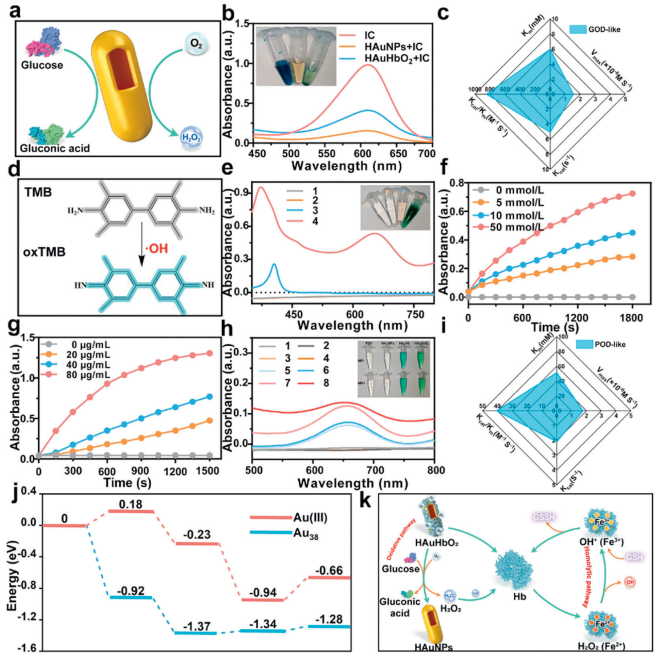


Fig. 2. Validation of the enzyme activities of $HAuHbO_2$. (a) Mechanism of H_2O_2 production by HAuNPs. (b) The generation of H_2O_2 was verified by IC. (c) GOD-like kinetic calculations for $HAuHbO_2$. (d) TMB to detect the reaction mechanism of $^{\bullet}OH$ generation. (e) UV absorption spectra of TMB incubated under PBS (1), TMB+Glu (2), TMB+$HAuHbO_2$ (3), and TMB+Glu+$HAuHbO_2$ (4). (f) Effect of different glucose concentrations on the production of $^{\bullet}OH$. (g) Effect of different concentrations of $HAuHbO_2$ on the generation of $^{\bullet}OH$. (h) Assay of the ability to generate $^{\bullet}OH$ under PBS (1), PBS+NIR (2), HAuNPs (3), HAuNPs+NIR (4), HAuHb (5), HAuHb+NIR (6), $HAuHbO_2$ (7), $HAuHbO_2$+NIR (8). (i) POD-like kinetic calculations for $HAuHbO_2$. (j) Free energy diagram of $HAuHbO_2$ in the process of glucose dehydrogenation to H_2O_2. (k) Mechanistic diagram of spontaneous cascade catalysis for $HAuHbO_2$.

Further, antitumor effects of $HAuHbO_2$ were explored in 4T1 tumor cells. The nanozyme labeled by the fluorescent dye Cy5.5 (Cy5.5+$HAuHbO_2$) were shown to accumulate over time in the cells (Fig. 3a). Flow cytometry also showed consistent accumulation of Cy5.5+$HAuHbO_2$ in cells (Fig. 3b). The localization of the

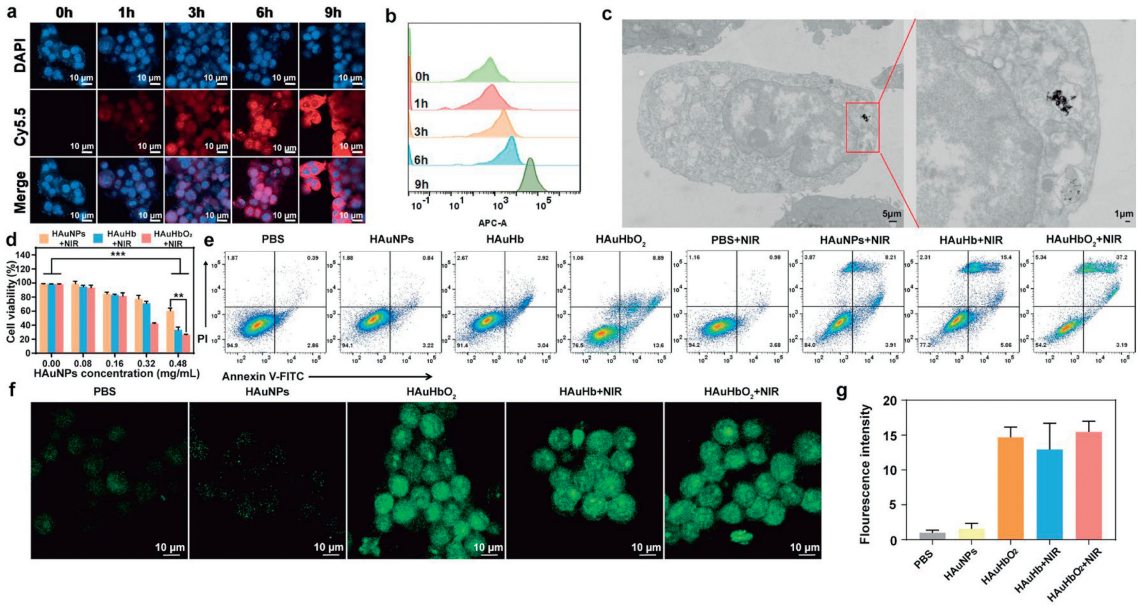


Fig. 3. Effects of $HAuHbO_2$ on 4T1 tumor cells. (a) Confocal laser scanning microscopy (CLSM) images of 4T1 cells interact with Cy5.5+$HAuHbO_2$ at different time points. Scale bar: 10 μm. (b) Flow cytometry analyses of red fluorescence levels of 4T1 cells incubated with Cy5.5+$HAuHbO_2$ at different time points. (c) Bio-TEM examination of the position of $HAuHbO_2$ in the 4T1 cells. (d) The cell counting kit-8 (CCK-8) technique assesses cell viability under laser. (e) Flow cytometry was used to analyze the apoptosis of cells. (f) The production of ·OH in 4T1 cells was analyzed by CLSM after different treatments. Scale bar: 10 μm. (g) Quantification of ·OH fluorescence in 4T1 tumor cells. All data were presented as means ± SEM ($n = 3$). $^{**}P < 0.01$, $^{***}P < 0.001$.

nanozyme in the cells was captured by bio-electron microscopy (Fig. 3c). All experimental results confirmed that $HAuHbO_2$ could be effectively phagocytosed by the cells. The cytotoxicity of $HAuHbO_2$ was further investigated. As shown in Fig. S9 (Supporting information), HAuNPs maintained a survival rate of >80 % at concentrations of 0–0.48 mg/mL, indicating that the nanozyme has almost no harmful effects on tumor cells with good biosafety. HAuHb and $HAuHbO_2$ showed destructive effects on tumor cells, possibly caused by the spontaneous cascade catalytic reaction. The nanozyme demonstrated excellent antitumor effects after laser irradiation (Fig. 3d). In order to prove the synergistic ability of catalytic therapy and PTT, the combination index (CI) was calculated. The results showed a CI of 0.822 indicating synergistic efficacy of nanozyme. Calcein-AM/PI staining studies demonstrated a direct visualization of 4T1 cells in each group. The strongest red fluorescence of $HAuHbO_2$ after laser can be seen in Fig. S10 (Supporting information). Apoptosis of cells in each group was detected by flow cytometry using Annexin V-FITC/PI kit. $HAuHbO_2$+NIR group having the highest mortality rate of 37.2 %. The results of the three assays consistently verified the biosafety and effective antitumor results of $HAuHbO_2$. Finally, 2′,7′-dichlorofluorescein diacetate (DCFH-DA) was used to track ·OH in tumor cells. The green fluorescence signals of HAuNPs, HAuHb, and $HAuHbO_2$ groups were gradually enhanced (Figs. 3f and g), indicating the production of ·OH in tumor cells.

Considering the above superior spontaneous cascade catalytic properties and antitumor effects of $HAuHbO_2$, its therapeutic properties *in vivo* were investigated. All animal studies were approved by the Ethics Committee of the Laboratory Animal Center of Guangdong Medical University (No. GDMU-2023–00,010) and followed the guidelines for using laboratory animals in Guangdong Province. Firstly, the biosafety of $HAuHbO_2$ was investigated using healthy mouse blood. As illustrated in Fig. S11 (Supporting information), no apparent hemolysis was induced and the hemolysis rates among these groups incubated with $HAuHbO_2$ at various concentrations were all below the standard level of 5 %, suggesting favorable hemocompatibility of nanozyme. Then, the biodistribution of $HAuHbO_2$ was further performed. As shown in Fig. S12 (Supporting information), the fluorescence signals of $HAuHbO_2$ at the tumor sites were significantly higher than in the free Cy5.5 group at each time point (Figs. S12a and b). The fluorescence of free Cy5.5 group was rapidly metabolized after 8 h of injection. In contrast, the nanozyme group maintained the fluorescence signal longer, indicating that $HAuHbO_2$ has a strong accumulation capacity at the tumor site. Fig. S12c demonstrates the fluorescence imaging of tumor tissues and major organs obtained from the mice at 24 h. The figure clearly shows that the fluorescence of free Cy5.5 group is not obvious, while the fluorescence of the $HAuHbO_2$ group is visible. It further shows that the nanozyme have good accumulation in mice. A consistent conclusion can also be obtained from the quantitative fluorescence analysis of Fig. S12d. Based on the absorption properties of $HAuHbO_2$ in the NIR II region, PA imaging was also used to verify the accumulation of $HAuHbO_2$ at mouse tumor sites. There was no obvious photoacoustic signal in the tumor region before $HAuHbO_2$ was injected (Fig. S12e). After 1 h of injection, the PA signal gradually enhanced and reached the highest value at the 8th hour (Fig. S12f). At 24 h after injection, the PA signal decreased rapidly and became undetectable. These experimental results demonstrated the ability of the $HAuHbO_2$ to accumulate at the tumor site. They enabled the determination of the occurrence of PTT at the appropriate time point, which is 8 h after injection.

In addition, the PA imaging system (850 nm) detected the oxygenated Hb (HbO_2) in the tumor vasculature during the accumulation of nanozyme. Fig. S12g demonstrates the signals of HbO_2 in the tumor site at 0 and 8 h after HAuHb and $HAuHbO_2$ were injected into mice, respectively. It was found that the PA signal in the HAuHb group did not enhance with time. On the contrary, the signal of HbO_2 in the $HAuHbO_2$ group was similar to the accumulation of nanozyme, and the PA signal reached a maximum after 8 h. It was also illustrated by the quantitative analysis of the HbO_2 signal (Fig. S12h). Therefore, it was concluded that $HAuHbO_2$ can carry O_2 into the tumor site, which allows spontaneous cascade reaction and relief of tumor hypoxia at the tumor site.

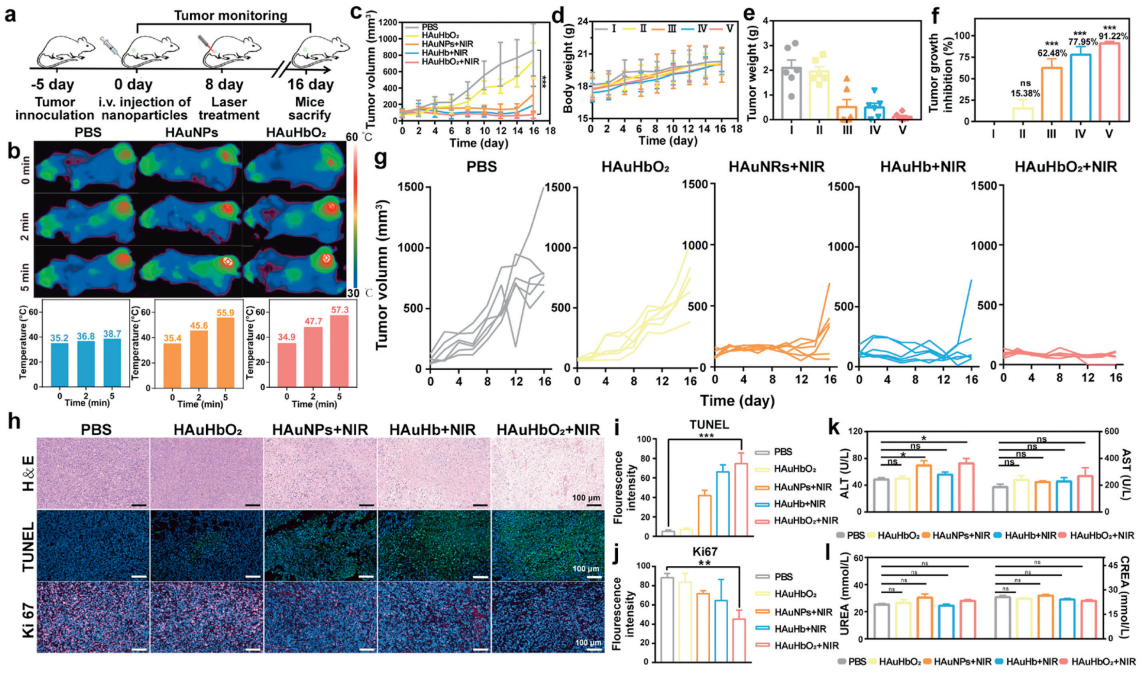


Fig. 4. Effects of $HAuHbO_2$ treatment on tumors *in vivo*. (a) Schematic illustration of $HAuHbO_2$ therapy procedure. (b) Temperature changes of tumor site under laser in mice treated with PBS, HAuNPs, and $HAuHbO_2$. (c) Tumor volumn changes during treatment with different materials. Body weight monitoring (d), tumor weight (e) and tumor growth inhibition rate (f) of different groups including PBS (I), $HAuHbO_2$ (II), HAuNRs+NIR (III), HAuHb+NIR (IV), and $HAuHbO_2$+NIR (V). (g) Tumor growth curves of every group. (h) H&E, TUNEL, and Ki67 immunofluorescence analysis of tumor sites in mice. Scale bar: 100 μm. (i–l) Fluorescence quantitative analysis of (i) TUNEL and (j) Ki67. The concentrations in serum of alanine aminotransferase (ALT) and aspartate aminotransferase (AST) (k), serum urea nitrogen (UREA) and creatinine (CREA) (l) after treatment. All data were presented as means ± SEM ($n = 6$). $^*P < 0.05$, $^{**}P < 0.01$, $^{***}P < 0.001$. ns: no significant.

According to the $HAuHbO_2$ accumulation in mice, the antitumor effects were further explored (Fig. 4a). An infrared thermography camera was used to record the temperature of tumor site and take thermography photos (Fig. 4b and Fig. S13 in Supporting information). The tumor sites of the mice in the PBS group did not show significant temperature changes (temperature change of 3.5 °C). In contrast, HAuNPs group and $HAuHbO_2$ group were heated significantly: the temperatures could reach 55.9 and 57.3 °C. It demonstrated the safe radiation of 808 nm laser and the better photothermal transduction ability of nanozyme, making it sufficient proof for happening of PTT. After, tumor volume and mouse weight were recorded. In Fig. 4c, the tumor volume of the mice in the PBS group showed a significant trend of increase. In contrast, the tumor growth in the $HAuHbO_2$ group was moderate, which likely attributed to the induction of CDT by the spontaneous cascade reaction of nanozyme. HAuHb+NIR and $HAuHbO_2$+NIR groups significantly inhibited tumor growth after treatment, and the $HAuHbO_2$+NIR group could even decreasing tumor volume. It indicates that the synergy of $HAuHbO_2$ with PTT and CDT *in vivo* could increase therapeutic effects. In Fig. 4d, the body weight of the mice in all groups showed an increasing trend within 16 days of treatment, indicating that the mice were growing normally, and the nanozyme had a reasonable level of biosafety. The serum, tumor tissues, and major organs were collected after 16 days of treatments. Fig. 4e and Fig. S14 (Supporting information) showed tumor weight and the excised tumors photo, from which the tumor inhibitory effects of the formulations in each group could be visualized. The tumor growth inhibition rate also demonstrated the antitumor ability of the nanozyme (Fig. 4f). $HAuHbO_2$ was not only catalyzed by cascade to undergo Fenton reaction but also achieved 91.22 % tumor inhibition under light-induced thermotherapy. Individual tumor growth curves revealed that tumors in the $HAuHbO_2$+NIR group may be completely eliminated (Fig. 4g). The effects of the nanozyme on tumor cell proliferation, apoptosis, and necrosis were further evaluated by histological analysis and immunofluorescence staining. In hematoxylin-eosin (H&E) staining of Fig. 4h, the cells in the tumor tissues with $HAuHbO_2$+NIR treatment showed deformation, nuclear shrinkage, and necrosis, while the morphology of the PBS group remained normal. The results of terminal-deoxynucleotidyl transferase mediated nick-end labeling (TUNEL) staining showed the strong green fluorescence in $HAuHbO_2$+NIR group, indicating the highest degree of apoptosis. Ki67, as a cell proliferation marker, was used to detect the proliferative ability of tumor cells. It was found that PBS group had obvious fluorescence signals. In contrast, the fluorescence intensity decreased rapidly after nanozyme treatment, indicating that nanozyme inhibited tumor cell proliferation (Fig. 4i) and increased apoptosis (Fig. 4j). Caspase-3 and Bcl-2 are important indicators of apoptosis, so the expression of these two proteins in tumor tissue was also evaluated. As shown in Fig. S15 (Supporting information), caspase-3 in tumor tissue was the highest in $HAuHbO_2$ + NIR group (Fig. S15a), indicating the possibility of subsequent induction of apoptosis. Bcl-2 as an anti-apoptotic protein, its expression can be seen in the figure to be the lowest in the final group. The results of immunofluorescence quantitative analysis show that nanozyme has a significant therapeutic effect on tumor (Figs. S15b and c).

Subsequently, the biosafety of $HAuHbO_2$ was verified *in vivo*. The biosafety of nanozymes can be inferred from Fig. S16 (Supporting information) that no significant damage was observed in the organs of the nanozyme groups compared to the control group. The nanozymes showed non-toxic effects on normal tissues while causing tumor cell death. The liver and kidney function indicators in the serum of the nanozyme groups were also not found to be significantly changed compared with the PBS group (Figs. 4k and l), confirming the biosafety of the nanozymes.

The antitumor mechanism of $HAuHbO_2$ was further explored. The studies and conclusions of previous studies provide potential mechanisms for the antitumor effects of $HAuHbO_2$ [23,24].

Firstly, the generation of ·OH by nanozymes was confirmed *in vivo*. DCFH-DA was used to detect ·OH at the tumor site. As shown in Fig. S17 (Supporting information), no green fluorescence was observed in the PBS group, while $HAuHbO_2$+NIR showed a clear fluorescence signal (Fig. S17a). This confirmation of ·OH generation would provide the possibility that $HAuHbO_2$ induces oxidative stress to cause immunogenic cell death (ICD). Subsequently, the occurrence of ICD was verified. Calreticulin (CRT) exposure and high - mobility group box 1 (HMGB1) exocytosis is important indicators for ICD development. The expression levels of CRT and HMGB1 in tumor tissues analyzed using immunofluorescence are shown in Fig. S17b. The fluorescence intensity of CRT with the $HAuHbO_2$+NIR treatment showed the highest level. Meanwhile, the fluorescence of HMGB1 in the PBS group was concentrated in the nucleus and had the highest fluorescence intensity. The expression of HMGB1 was weakened in the other groups as the drug's efficacy was enhanced. Both CRT exposure and HMGB1 exocytosis results demonstrated the occurrence of ICD. Then, the stimulation of dendritic cell (DC) maturation by damage-associated molecular patterns (DAMPs) was analyzed using flow cytometry [25,26]. The maturity of DCs was determined by detecting the number of $CD80^+$ $CD86^+$ DCs. As shown in Fig. S18 (Supporting information), the maturation percentage of DCs in the PBS group was 5.63%, and in the $HAuHbO_2$+NIR group could reach 9.65%, which was 1.71 times higher than that in the PBS group (Fig. S18a). It demonstrated that laser-mediated $HAuHbO_2$ promotes the maturation of DCs to present antigens to T cells for specific immune responses. Consequently, the proportion of T cells was also assayed. CD3 is often used to differentiate between helper T cells ($CD3^+$ $CD4^+$ Tc) and killer T cells ($CD3^+$ $CD8^+$ Tc). Fig. S18b shows the proportion of $CD3^+$ $CD4^+$ and $CD3^+$ $CD8^+$ Tc in tumor tissues. The highest percentages were found in the group treated with $HAuHbO_2$+NIR, which was 11.42- and 6.46-fold higher than in the PBS group, respectively. The expression levels of CD4 and CD8 in tumor tissues were detected by immunofluorescence, and differences across different treatment groups were consistent with the above analysis (Fig. S19 in Supporting information). In addition to activating T cells to attack tumors, mature DCs also induced the release of interferon-γ (IFN-γ), thereby stimulating T cells to differentiate into tumor-specific IFN-γ T cells (IFN-γ^+Tc). In Fig. S18c, the proportion of IFN-γ^+Tc in tumor tissues in the PBS group was 3.49%. $HAuHbO_2$+NIR increased the proportion of IFN-γ^+ Tc to 11.5% (3.29-fold).

In addition, a major challenge in tumor immunotherapy is the development of immune tolerance or immunosuppression by the tumors due to the fact that tumor cells release cytokines to summon Treg cells [27,28]. Therefore, the presence of Treg cells is an important indicator of tumor immunoassay [29]. The number of $CD3^+$ $CD4^+$ $Foxp3^+$ Tc was examined. As shown in Fig. S18d, the percentage of Treg cells in the PBS group was 9.30%, and in the $HAuHbO_2$+NIR group decreased to 2.15%. The expression of Foxp3 in the tumor tissues of each group is also clearly shown in Fig. S19 (Supporting information), in which there was no significant expression of Foxp3 in the nanozyme group. These results indicate that nanozymes assisted by NIR laser could effectively reduce the number of Treg cells in tumor tissues. When the immune response of the organism is activated, the secretion of immune-related factors (interleukin (IL)-12, tumor necrosis factor (TNF)-α, *etc.*) in tumor tissues increases, activating T cells to kill tumor cells [30–32]. As shown in Fig. S20 (Supporting information), the highest levels of TNF-α, IL-12, and IFN-γ were found in the $HAuHbO_2$+NIR group. In conclusion, $HAuHbO_2$ with NIR laser irradiation can induce ICD and significantly promote the maturation of DCs to activate immunity. At the same time, it can promote the infiltration of T cells within the tumor and reduce the number of Treg cells, resulting in decreased immunosuppression.

This study reports $HAuHbO_2$ nanozyme that can be used as an antitumor preparation with multiple functions and catalyzed by spontaneous cascades. The specific spatial arrangement of the hollow gold rods enables the nanozyme to possess GOD-like enzymatic activity and excellent photothermal conversion ability. The loaded Hb, as a natural protein, plays a POD-like role in the nanozymatic system, providing the raw material for the Fenton reaction for CDT and promoting the antitumor therapy of the nanozyme by its own oxygen-carrying function. $HAuHbO_2$ displays an efficient ·OH-generating capacity in the tumor microenvironment to induce apoptosis in tumor cells. The spontaneous cascade catalysis and the synergistic effect with PTT activate the ICD effect in tumors. By promoting DC maturation, stimulating T cell activation, inhibiting the number of Treg cells, and increasing cytokine secretion, the antitumor immune response was enhanced, ultimately inhibiting tumor growth. In addition, $HAuHbO_2$ can exert self-sufficiency, circulating reactants and products, and exert maximum value by making the best use of its components at the tumor site. Overall, the nanozyme reported in this study will provide great potential for clinical cancer therapy.

Declaration of competing interest

The authors declare that they have no known competing financial interests or personal relationships that could have appeared to influence the work reported in this paper.

CRediT authorship contribution statement

Dou Zhang: Writing – review & editing, Writing – original draft, Visualization, Software, Project administration, Methodology, Formal analysis, Data curation, Conceptualization. **Xinyi Cai:** Methodology, Formal analysis, Data curation, Conceptualization. **Yimin Li:** Funding acquisition. **Yong Liu:** Methodology, Formal analysis. **Long Qiu:** Visualization, Methodology. **Zhenying Diao:** Formal analysis, Data curation. **Xuyi Liu:** Software, Methodology. **Yuta Nishina:** Methodology, Formal analysis, Data curation. **Yajuan Zou:** Methodology, Formal analysis, Data curation. **Jianbo Sun:** Validation, Data curation. **Shujing Liang:** Supervision, Funding acquisition. **Daxiang Cui:** Supervision, Methodology, Funding acquisition, Data curation, Conceptualization. **Ting Yin:** Writing – review & editing, Visualization, Supervision, Resources, Methodology, Funding acquisition, Data curation, Conceptualization.

Acknowledgments

This work was funded by Natural Science Foundation of Guangdong Province (No. 2024A1515030063), Construction Project of Nano Technology and Application Engineering Research Center of Guangdong Medical University (No. 4SG25008G), Discipline Construction Project of Guangdong Medical University (No. 4SG24015G), Funds for PhD researchers of Guangdong Medical University in 2024, National Natural Science Foundation of China (Nos. 82160478, 81703075) and Dongguan City Social Development Science and Technology Key Project (No. 20221800906362).

Supplementary materials

Supplementary material associated with this article can be found, in the online version, at doi:10.1016/j.cclet.2025.111569.

References

[1] S. Srinivasan, T. Kryza, J. Batra, et al., Nat. Rev. Cancer 22 (2022) 223–238.
[2] M. De Martino, J.C. Rathmell, L. Galluzzi, et al., Nat. Rev. Immunol. 24 (2024) 654–669.

[3] C. Pan, B. Li, M. Simon, Mol. Cell 81 (2021) 3760–3774.
[4] S. Tang, Y. Wang, R. Luo, et al., Nat. Commun. 15 (2024) 1381.
[5] H. Jin, J. Wang, Z. Wang, et al., J. Hematol. Oncol. 16 (2023) 103.
[6] H. Zhang, Y. Li, J. Huang, et al., Acta Pharm. Sin. B 14 (2024) 4717–4737.
[7] L. Yang, Z. Chu, M. Liu, et al., J. Hematol. Oncol. 16 (2023) 59.
[8] L. Zhou, X. Lin, J. Zhu, et al., Cell Death Discov. 9 (2023) 23.
[9] A. Petruzzella, M. Bruand, A. Santamaria-Martínez, et al., Nat. Chem. Biol. 20 (2024) 1188–1198.
[10] J. Wang, Y. Yang, F. Shao, et al., Nat. Metab. 6 (2024) 914–932.
[11] Q. Duan, Y. Zhu, B. Shan, et al., Adv. Funct. Mater. 33 (2023) 2213636.
[12] Y. Zhang, S. Jiang, J. Lin, et al., Angew. Chem. Int. Ed. 61 (2022) e202208583.
[13] S. Galanie, D. Entwistle, J. Lalonde, Nat. Prod. Rep. 37 (2020) 1122–1143.
[14] R. Tanifuji, A. Minami, H. Oguri, et al., Nat. Prod. Rep. 37 (2020) 1098–1121.
[15] Y. Huang, J. Ren, X. Qu, Chem. Rev. 119 (2019) 4357–4412.
[16] Y. Xing, F. Yasinjan, S. Sun, et al., Nano Today 57 (2024) 102386.
[17] J. Shen, J. Chen, Y. Qian, et al., Adv. Mater. 36 (2024) e2313406.
[18] Y. Liu, B. Wang, J. Zhu, et al., Adv. Mater. 35 (2023) e2208512.
[19] P. Ghaffari-Bohlouli, H. Jafari, L. Nie, et al., Adv. Healthc. Mater. 13 (2024) e2401713.
[20] U. Kim, J. Song, D. Lee, et al., Biosens. Bioelectron. 74 (2015) 469–475.
[21] H. Kim, J. Yoon, H.K. Kim, et al., Bioact. Mater. 22 (2023) 112–126.
[22] J. He, Z. Li, P. Feng, et al., Angew. Chem. Int. Ed. 63 (2024) e202410381.
[23] L. Xin, F. Xiong, X. Cao, et al., Chin. Chem. Lett. 37 (2026) 110970.
[24] Y. Qin, H. Zhang, Y. Li, et al., Macromol. Biosci. 23 (2023) e2300093.
[25] T. Nie, Y. Fang, R. Zhang, et al., Bioact. Mater. 11 (2025) 51–63.
[26] J. Liu, G. Liu, C. Dai, et al., Chem. Eng. J. 485 (2024) 149446.
[27] Y. Yan, L. Huang, Y. Liu, et al., J. Hematol. Oncol. 15 (2022) 104.
[28] C. Tay, A. Tanaka, S. Sakaguchi, Cancer Cell 41 (2023) 450–465.
[29] R. Zheng, Z. Chen, Q. Li, et al., Chin. Chem. Lett. 36 (2025) 110865.
[30] G. Dranoff, Nat. Rev. Cancer 4 (2004) 11–22.
[31] D. Briukhovetska, J. Dörr, S. Endres, et al., Nat. Rev. Cancer 21 (2021) 481–499.
[32] D.J. Propper, F.R. Balkwill, Nat. Rev. Clin. Oncol. 19 (2022) 237–253.